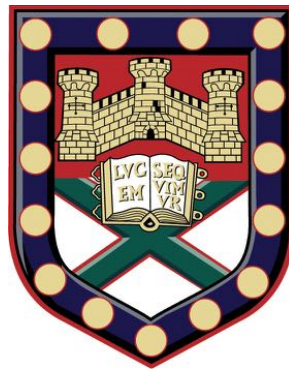


# Two dimensional atomically thin materials and hybrid superconducting devices



David Christopher Hudson

School of Physics

University of Exeter

A thesis submitted for the degree of

Doctor of Philosophy in Physics

September 2014

# Two dimensional atomically thin materials and hybrid superconducting devices

Submitted by David Christopher Hudson to the University of Exeter as  
a thesis for the degree of Doctor of Philosophy in Physics.

September 2014

This thesis is available for library use on the understanding that it is copyright material  
and that no quotation from the thesis may be published without proper acknowledge-  
ment.

I certify that all material in this thesis which is not my own work has been identified  
and that no material has previously submitted and approved for the award of a degree  
by this or any other university.

David Christopher Hudson

September 2014

## Abstract

In this thesis a variety of topics concerning 2D materials that have been separated from bulk layered crystals are discussed. Throughout the thesis, single and few layers of graphene, fluorinated graphene, MoS<sub>2</sub> and WS<sub>2</sub> are used. Two new methods of freely suspending 2D materials are presented as well as a method of removing the background from optical images. This aids contrast measurements for the determination of the number of layers.

Fluorinated graphene is found to be sensitive to beta radiation; the resistance of fluorinated graphene transistors is shown to decrease upon exposure to the radiation. This happens due to the carbon-fluorine bond breaking. The  $sp^3$  hybridised structure of the fluorinated graphene is reduced back into the  $sp^2$  hybridised structure of pristine graphene.

The superconducting properties of molybdenum-rhenium are characterised. It is shown to have a transition temperature of 7.5 K. It is also discovered that the material has a resistance to hydrofluoric acid; the acid etches nearly all other superconducting materials. This makes MoRe a possible candidate to explore superconductivity in conjunction with high mobility suspended graphene. To see if the material is compatible with graphene, a supported Josephson junction is fabricated. A proximity induced super current is sustained through the junction up to biases of  $\sim 200$  nA.

The temperature dependence of the conductivity is measured for both suspended MoS<sub>2</sub> and WS<sub>2</sub> on a hexagonal boron nitride substrate. The dominant hopping mechanism that contributes to the conductivity at low temperatures is found to be Mott variable range hopping, with the characteristic  $T^{-1/3}$  dependence. The hopping transport is due to impurities that are intrinsic to the crystals, this is confirmed by comparing the results with those of supported devices on SiO<sub>2</sub>.

## Acknowledgements

First I would like to say thanks to my supervisor Saverio Russo. It was clear from the beginning to see the passion and dedication he has for not only research, but also family. I would also like to thank Monica Craciun for useful discussions. I have learnt a great deal from both of them and I put that down to the working environment they created, which feels like a family. Everyone looking out for and helping each other, while also striving to do the best work possible each time. A big thank you to Russo and Craciun lab members past and present: Tymofiy Khodkov, Ivan Khrapach and Freddie Withers, who were already in the group when I joined and along with Saverio taught me everything I know about fabrication and measurement techniques. Steve Martins, Mohsin Aziz, Selim Unal, Mukond Khetani, Gareth Jones, Dominique Wehenkel, Matthew Barnes, Adolfo De-Sanctis it has been a pleasure working with you and even more so when not working! A special thanks to other PhD students, Sam Hornett, Claire Woollacott, Luke Coombes, Chris Downs, Charles Downing, Sneha Eashwer-Singhraj, Lachlan Marnham, Alex Pettitt, Damian Rumble, Hannah Wakeford and countless others for making my experience in Exeter a great one.

I would like to thank all my collaborators and highlight specific contributions to this thesis. Chris Downs for always being available to put his life in mortal danger and pour hydrofluoric acid over my devices. Marc Dubois for providing the technical knowledge and means of fluorinating graphite. Matthew Barnes for transferring CVD graphene and fabricating a device for chapter 4. Steve Martins for his initial measurements of the exfoliated fluorinated graphene devices. Freddie Withers for measurements on  $WS_2$  and immensely improving my understanding of hopping conduction. Thomas Bointon for his help in Raman and AFM characterisation of devices.

I would also like to thank the technical, experimental officers and academic staff

at the University, without who this thesis would not be possible. Thank you to Adam Woodgate and David Gregory who supply liquid helium for measurements and are always available for a chat. To Paul Wilkins who has helped me cut many, many pieces of metal and wood for the most obscure purposes. His help has propped up my research both literally and figuratively and he is never too busy to help. I would like to thank David Anderson whose expert knowledge on electron beam lithography has been invaluable, he always has a solution and the time to help. To Mark Heath for keeping the cleanroom in perfect working order and providing assistance whenever possible. A special mention to David Horsell for his knowledge of cryogenic systems and guidance when cooling down a cryostat. To Alan Usher, my masters supervisor, whose project sparked my interest in condensed matter physics.

Finally a thanks to my closest friends and family for their constant support. My friends who have been with me since my undergraduate degree, many of whom I have lived with, Thomas Bointon, Alex Pearce, Thomas Haworth, Adam Snitch, Nikeel Patel. The shared experiences of our time in Exeter will stay with me forever. To my parents, Chris and Bridgit for their love and unwavering support; my brothers, Robbie and Sam; and to Sophie Worsfold, who has stuck by my side and provided constant motivation to help me finish my PhD.

All the best to everyone in the Russo-Craciun team and I hope to read many more papers from these wonderful people in the future.

## List of publications

Electrical transport in suspended and double gated trilayer graphene. T. Khodkov, F. Withers, D. C. Hudson, M. F. Craciun and S. Russo, *Appl. Phys. Lett.* **100**, 013114 (2012)

Electron transport of WS<sub>2</sub> transistors in a hexagonal boron nitride dielectric environment. F. Withers, T. H. Bointon, D. C. Hudson, M. F. Craciun and S. Russo, *Scientific Reports* **4**, 4967 (2014)

Molybdenum-Rhenium superconducting suspended nanostructures. M. Aziz, D. C. Hudson, and S. Russo, *Appl. Phys. Lett.* **104**, 233102 (2014)

Beta radiation detection using fluorinated graphene. D. C. Hudson, M. D. Barns, S. E. Martins, M. Dubois, and S. Russo (in preparation)

# List of Figures

- 2.1 The crystal lattice and Brillouin zone in graphene: **a)** The hexagonal lattice of a single graphene sheet is divided into two sub lattices with inequivalent atoms labelled A and B. The sub lattice vectors are labelled  $\mathbf{a}_1$  and  $\mathbf{a}_2$ , the nearest neighbour vectors  $\boldsymbol{\delta}_1$ ,  $\boldsymbol{\delta}_2$  and  $\boldsymbol{\delta}_3$ . The dashed diamond indicates the primitive unit cell of the lattice. **b)** The Brillouin zone scheme: high symmetry points are labelled such as the zone centre ( $\Gamma$ ); the mid-point of a zone edge ( $\mathbf{M}$ ); and corners of the Brillouin zone ( $\mathbf{K}$ ) and ( $\mathbf{K}'$ ). The Brillouin zone vectors are labelled  $\mathbf{b}_1$  and  $\mathbf{b}_2$ . . . . . 12
- 2.2 The band structure of monolayer graphene: **a)** The  $\pi$  and  $\pi^*$  bands as a function of  $k_x$  and  $k_y$ . The two bands meet at six points in the Brillouin zone where  $E(\mathbf{k}) = 0$ . A zoom around of one of these points is shown next to the main panel highlighting the linear dispersion. **b)** A trace of  $E(\mathbf{k})$  along the high symmetry points  $\Gamma - \mathbf{M} - \mathbf{K}$ , notable is the asymmetry between the  $\pi$  and  $\pi^*$  bands due to the non-zero wave function overlap parameter  $s_0$ . . . . . 18

- 2.3 Fluorinated graphene: **a)** A 3D representation of the crystal lattice (upper [8]) and isometric (lower). The grey atoms are carbon and the green atoms are fluorine. The  $sp^2$  hybridization of graphene is modified by the attachment of the fluorine atoms and a 3D  $sp^3$  structure is obtained. The angle between a carbon atom and two nearest neighbours is decreased to  $\sim 110^\circ$  as the structure is transposed up and down on adjacent sites. **b)** The band structure of fully fluorinated graphene as calculated from first principles [7]. There is a band gap at the  $\Gamma$ -point of around 3.5 eV. 21

- 2.4 The trigonal prismatic structure of the TMDs: here atom  $a$  is a chalcogen and atom  $b$  is a transition metal. **a)** 3D view of the van der Waals stacked layers [14]. **b)** A side and top view of the hexagonal arrangement of the atoms [15]. **c)** The left panel shows the band structure of bulk  $\text{MoS}_2$ ; there is an indirect transition at the  $\Gamma$  point. The band structure of monolayer  $\text{MoS}_2$  is shown in the right panel; there is a direct transition at the K-point [16]. Note that the band structure of  $\text{WS}_2$ , although not shown, has similar features to  $\text{MoS}_2$ . The Hartree is the atomic unit of energy, where  $1E_{\text{Hartree}} \sim 27.2$  eV. . . . . 23



- 2.5 Spin orbit splitting in TMDs: Spin split bands of monolayer **a)** MoS<sub>2</sub> and **b)** WS<sub>2</sub>. The dashed red lines indicate the band structure calculated without the spin orbit interaction and the solid black lines with spin orbit interaction [17] There is a large splitting at the K-point in the valence band for both cases but the splitting size in WS<sub>2</sub> > MoS<sub>2</sub>. The conduction band at the K-point becomes doubly degenerate. **c)** The allowed optical transitions from the valence bands of the K and K' valleys to the conduction band. Time reversal symmetry between the same bands in adjacent K-points leads to opposite spin split populations in each valley (indicated by the dashed and solid lines)[19]. . . . . 25
- 2.6 **a)** A depiction of the impurity bands that are introduced due to doping in a semiconductor. The transition from the lowest filled impurity band to the conduction band is labeled  $\epsilon_{act}$  and the width of this band is  $\epsilon_{nh}$ . **b)** The temperature dependence of the conductivity in a lightly doped semiconductor, plotted logarithmically as a function of  $T^{-1}$ . Region A corresponds to the intrinsic conductivity of the semiconductor at high temperatures. Regions B to D are due to the extrinsic conductivity governed by the specific nature of the impurities, as described in the main text. Modified from [21]. . . . . 26

- 2.7 **a)** An illustration of the density of states  $g(\epsilon)$  in a highly disordered semiconductor. The continuous region of states within the forbidden region is known as the mobility gap. This separates the extended states of the conduction and valence bands from the localised states in the gap. **b)** A comparison of the nearest neighbour hopping (blue) and variable range hopping (red). At low temperatures it may require less energy for an electron to hop to a state at a further distance. **c)** A band of states with width  $2\epsilon_0$  around the Fermi level in the centre of the mobility gap. These states will contribute to the variable range hopping. A constant density of states is assumed close to  $E_F$ . . . . . 29
- 2.8 Types of Raman scattering: **a)** Elastic Rayleigh Scattering, a photon excites an electron into a virtual level which then decays and emits a photon of the same energy. **b)** Stokes and **c)** anti-Stokes, Inelastic, non-resonant scattering. After excitation with a photon to a virtual state the electron will emit (Stokes) or absorb (anti-Stokes) a phonon before decaying and emitting a photon of different energy. **d)** Stokes and **e)** anti-Stokes, inelastic resonant scattering. In these cases it is the same for **b)** and **c)** except that the incident photon has an energy that matches a transition to a real unoccupied electronic state. The resonant scattering processes produce more prominent peaks in the Raman spectra of the 2D materials. Adapted from [27]. . . . . 32

- 
- 2.9 **a)** Phonon dispersion of monolayer graphene. Red circles identify the locations of the main Raman active phonon modes as described in the main text, adapted from [28]. **b)** Raman spectra of pristine graphene (top) and defected graphene (bottom). [27] **c)** Outlines of the different Raman scattering processes in monolayer graphene, adapted from [29] . 34
- 2.10 The single electron density of states and filled energy levels for **a)** a typical normal metal and **b)** a BCS superconductor. In the density of states for the superconductor at the Fermi level there is a delta function (labelled CP) representing the quasi-particle Cooper pair density of states. 39
- 2.11 Andreev reflection: **a)** An electron in a normal metal lead impinging upon the superconductor interface with energy  $E_F + \epsilon$  where  $\epsilon < \Delta$ . **b)** The charge transfer process at the interface during Andreev reflection; a total charge of  $2e$  is transferred to the superconductor. Electrons are shown as filled black circles and holes as outlined circles. . . . . 40
- 2.12 Andreev reflection in a SNS junction. Electrons are represented by filled black circles, holes by outlined circles. . . . . 42
- 2.13 Reflection processes between: **a)** A normal metal and an insulator; an electron is specularly reflected back into the normal metal. **b)** A normal metal and a superconductor or doped graphene and a superconductor; an electron undergoes Andreev reflection and a hole is retro-reflected. **c)** Undoped graphene and a superconductor; the Andreev reflection process is specular meaning the hole is specularly reflected. Adapted from [44]. 45

- 3.1 Standard electron beam lithography procedure for depositing metallic contacts: **a)** After spin coating PMMA resist, it is exposed to electron beam irradiation defining a pattern for metallic contacts. **b)** The exposed regions are removed by developing in MIBK for 20 seconds. **c)** The metals for the contacts are evaporated onto the substrate; a discontinuous film is achieved by the developed regions. **d)** The unwanted metal can be removed by dissolving the remaining PMMA in acetone. . . 53
- 3.2 Hydrofluoric acid etching process: **a)** A schematic showing the supported sample after metallic contact deposition but before the etching process. **b)** The device is placed in a buffered HF solution for 2.5 mins, which etches 200 nm; then it is subsequently transferred to DI water then IPA. **c)** A view of an etched sample, the oxide layer is 300 nm thick, so a thin layer still remains after etching; however there is an undercut beneath the gold contacts. **d)** The IPA is heated to 60°C and then transferred to a glass slide on a hot plate. This causes the IPA to evaporate with low surface tension. **e)** SEM image of a suspended graphene device. . . 56

- 3.3 Cross-linked PMMA suspension process: **a)** PMMA is spun onto a SiO<sub>2</sub> substrate and then few layer flakes are mechanically exfoliated onto the PMMA. A ramp from the PMMA surface down to the SiO<sub>2</sub> is constructed by a varying low dose of e-beam exposure. **b)** The PMMA is developed in MIBK leaving the ramps in tact. A large dose is then applied to the ramps to cause them to cross-link as shown in **c)**. **d)** A new layer of PMMA is spun on top to fill the gaps and allow the standard procedure of e-beam lithography to take place in step **e)**. **f)** For the final lift-off step in acetone all of the PMMA will be removed except for the cross-linked regions. Depending on how thick the layer of cross-linked PMMA is, it may be necessary to dry the sample on a hotplate as in Fig. 3.2. **g)** Dose versus height calibration for the PMMA ramps. **h)** AFM measurement of a PMMA ramp courtesy of Thomas Bointon. **i)** SEM image of a finished device showing two suspended regions. . . . . 58
- 3.4 HSQ suspension process: **a)** HSQ is spun onto SiO<sub>2</sub> and few layer flakes are then mechanically exfoliated onto HSQ. A layer of PMMA is then spun on top of this structure and the regions defining the contacts are exposed by standard e-beam doses. **b)** The exposure cross-links the HSQ, so after the PMMA is developed the HSQ remains untouched. Metallic contacts can be deposited. **c)** The metal is removed by lift-off in acetone but this does not affect the unexposed HSQ. **d)** To remove the unexposed HSQ and suspend the flakes the sample is washed in MF 319. It is then dried on a hot plate as in Fig. 3.2. **f)** SEM image of a finished device. . . . . 60

3.5	Device annealing methods: <b>a)</b> Heating in a furnace at 200°C under either a hydrogen/argon atmosphere (pictured) or vacuum. <b>b)</b> Electrical circuit for current annealing. <b>c)</b> Back gate dependence of resistance for a graphene flake before and after current annealing [7]. . . . .	63
3.6	Representations of the $sp^2$ hybridised structure of graphene (left) and the $sp^3$ hybridised structure of fully fluorinated graphene (right). . . . .	64
3.7	<b>a)</b> An example of multiple graphene flakes of different thicknesses; ranked in order of increasing contrast. <b>b)</b> The measured average contrast of over 130 graphene flakes. There are clear plateaus distinguishing up to three layers. <b>c)</b> An example of a vignette that is subtracted from the optical images (the contrast has been modified to exaggerate the effect). . . . .	65
3.8	Raman spectra for graphene flakes of different layer numbers. The solid black lines are Lorentzian fits to the 2D-peak and the dashed black line is the final fit. Adapted from [17]. . . . .	68
3.9	Raman characterisation of TMDs. <b>a)</b> Phonon dispersion for monolayer MoS <sub>2</sub> (left) <b>b)</b> and WS <sub>2</sub> (right), adapted from [22]. <b>c)</b> Raman spectrum of bulk WS <sub>2</sub> , the peak at 350 cm <sup>-1</sup> is fitted to two Lorentzians corresponding to the $E_{2g}^1(\Gamma)$ and 2LA(M) modes; the peak at 420 cm <sup>-1</sup> corresponds to the $A_{1g}(\Gamma)$ mode [23]. <b>d)</b> The vibrational directions of the atoms for the $E_{2g}^1(\Gamma)$ mode (left), the 2LA(M) mode (centre) and the $A_{1g}(\Gamma)$ mode (right). <b>e)</b> Raman spectrum of WS <sub>2</sub> for increasing number of layers [23]. <b>f)</b> Peak positions of the Raman active modes for increasing layer count [23]. All Raman spectra in this figure were taken with a laser wavelength of 532 nm with a spot size of 1.5 μm and 1 mW incident power. . . . .	70

- 3.10 **a)** Gate voltage dependence of the resistivity  $R(V_g)$  for a monolayer graphene transistor device, adapted from [27]. **b)** Constant current circuit diagram for measuring  $R(V_g)$ . **c)** Gate voltage dependence of the source-drain current  $I(V_g)$  for a monolayer MoS<sub>2</sub> device, adapted from [28]. **d)** Constant voltage circuit diagram for measuring  $I(V_g)$ . . . . . 73
- 4.1 Decay Process for <sup>90</sup>Sr. The initial decay process into <sup>90</sup>Y has a half-life of  $\lambda = 28.5$  years and produces almost exclusively  $\beta$  radiation with an energy of 546 keV. These beta processes do not have enough energy to leave the radioactive source; the second decay process into <sup>90</sup>Zr produces much higher energy  $\beta$  particles  $\sim 2.3$  MeV. These particles have a high enough energy to leave the source and reach the sample. . . . . 81
- 4.2 **a)** False colour SEM image of a typical device. Yellow represents the Cr/Au contacts, purple is the SiO<sub>2</sub> substrate and the green areas are FG. **b)**  $I_{SD}$  as a function of bias voltage  $V_{bias}$  for a FG flake unexposed to beta radiation. **c)** Schematic of the experimental setup, the <sup>90</sup>Sr beta source exposes the surface of the FG flake to  $\beta^-$  particles. **d)** The structure of fully fluorinated graphene, before (left) and after (right) exposure. The blue atoms represent carbon and the yellow atoms represent fluorine. . . . . 83
- 4.3 Calibration of the Strontium-90 source: **a)** The number of counts recorded on a Geiger counter as a function of distance in air. The counts decrease at an exponential rate with distance. **b)** The normalised profile of the emitted beam from the source, the maximum emission angle is  $\sim 60^\circ$ . . . . . 85
- 4.4  $IV$  characteristics before (blue) and after (red) exposure to <sup>90</sup>Sr for: **a)** pristine graphene for 12 hours and **b)** FG for 30 minutes. **c)** The evolution of the  $IV$  curves for a FG device after exposure for 16 hours. . . . . 86

- 
- 4.5 The estimated resistance of the sample plotted against the exposure time/dose. The shaded regions indicate regimes with different defluorination rates (yellow higher/blue lower). Inset: A log-log plot of the high dose regime. The dose required to fully defluorinate the graphene is extracted from the fit. . . . . 89
- 4.6 CVD grown fluorinated graphene with dimensions  $L = 1 \text{ cm} \times W = 0.85 \text{ cm}$ : **a)** Photograph of the device on a flexible transparent substrate. **b)** Resistance as a function of exposure time/dose. . . . . 91
- 5.1 **a)** A 100 nm sputter deposition of MoRe with a 5 nm Pd sticking layer; 300 W power and 3 mTorr gas pressure. The blue outline corresponds to a region where e-beam contacts have been defined. **b)** Close up of the MoRe leads after lift-off in acetone showing defects. Below the images are side on representations of the current stage in the lithography process. 97
- 5.2 Characterisation of a 200 nm wide channel of MoRe: **a)** The temperature dependence of the resistance measured upon cooling the device. The superconducting transition temperature  $T_C = 5.67 \text{ K}$ . The inset is an optical image of the channel after successful MoRe deposition. **b)** The  $VI$  characteristics of the channel at 250 mK, arrows indicate the direction of the sweeps. The critical current  $I_C = 2.98 \text{ mA}$  and the re-trapping current  $I_R = 0.16 \text{ mA}$ . . . . . 99



- 5.3 Magnetic field dependence of the MoRe Channel: **a)** Downsweep and **b)** upswing colour plots of the voltage drop along the length of the channel as a function of source-drain current and magnetic field,  $T = 250$  mK. **c)** and **d)** are the same data as above but plotted in a signed binary colour scheme where positive values are red, zero values are green and negative values are blue. In the green regions the resistance of the device is  $0 \Omega$ . **e)** Left axis: The zero-bias resistance of the channel for increasing magnetic field. The critical field  $B_C \sim 8$  T. Right axis: The extracted values of  $I_C$  from the upswing measurements. **f)** The computed values of the critical field as a function of temperature. . . . . 101
- 5.4 Temperature dependence of the resistance for a  $250 \mu\text{m} \times 250 \mu\text{m}$  MoRe square with thickness 120 nm. The transition temperature where the resistance drops to  $0 \Omega$  is  $\sim 7.5$  K. . . . . 102
- 5.5 **a)** A false colour SEM image of a MoRe channel after HF etching. **b)** Voltage-current characteristics for the etched MoRe channel. . . . . 103
- 5.6 Characterisation of a Ti/MoRe (5 nm/120 nm) Josephson junction with graphene weak link of channel length 200 nm: **a)** An optical image of the device with multiple channel lengths (100, 150 & 200 nm). **b)** The gate voltage dependence of the resistance of the at  $\sim 270$  mK. The graphene is electron doped to only a few volts. **c)** The  $VI$  characteristics at a gate voltage of 0 V (blue curve) and 50 V (red curve) at  $T = 30$  mK. **d)** The differential resistance as a function of the source drain current. The dashed lines are a guide to match the features with the  $VI$  curve. . . 105

- 5.7 **a)** Temperature dependence of the differential resistance in the bias range  $\pm 50 \mu\text{A}$ .  $T$  increases from 280 mK (blue) to 13 K (red). Features of interest are labeled with Roman numerals; the inset is a zoom showing the evolution of the low bias peak that appears for low  $T$ . **b)** The differential resistance as a function of bias voltage for  $T = 280 \text{ mK}$ , labelled are the BCS predicted values of the superconducting gap  $\Delta$  for MoRe. All plots in this figure were taken at  $V_g = 0$ . . . . . 107
- 6.1 The dry transfer process for flakes: **a)** The substrate is prepared by first spinning a water soluble polymer (aquasave) on  $\text{SiO}_2$  and then a layer of PMMA.  $\text{WS}_2$  flakes are exfoliated onto the PMMA. **b)** A membrane is constructed using tape with a small square hole cut in the centre. The substrate is attached to the tape. **c)** The sample is exposed to water and the aquasave dissolves leaving the PMMA and flakes freely suspended over the hole in the tape. **d)** A second substrate is prepared with boron nitride flakes. The flakes on the membrane can be aligned over the boron nitride using an optical microscope and a height adjustable stage. The substrate is heated to melt the PMMA and complete the transfer process. 115
- 6.2 **a)**  $IV$  characteristics of a device before and after annealing. **b)** The circuit setup for annealing, a large  $1 \text{ G}\Omega$  resistor is placed in series to the device to prevent damage to the flake if the resistance drops sharply. 116
- 6.3 Field effect transfer characteristics for **a)** single layer  $\text{MoS}_2$  on  $\text{SiO}_2$ , **b)** 4-layer  $\text{MoS}_2$  on  $\text{SiO}_2$  and **c)** 4-layer  $\text{MoS}_2$  on h-BN. The device in **c)** has the largest mobility with  $\mu = 80 \text{ cm}^{-2}\text{V}^{-1}\text{s}^{-1}$ . The mobilities are calculated using the method described in chapter 3.4.2. . . . . 117

- 6.4 **a)** The temperature dependence of  $\sigma(V_g)$  for 4-layer WS<sub>2</sub> on h-BN. The temperature range is from 200 K down to 4.2 K over a narrow gate voltage range. **b)** The temperature dependence of  $\sigma(V_g)$  for 4-layer WS<sub>2</sub> on SiO<sub>2</sub>. An expanded gate voltage range is shown. . . . . 118
- 6.5 Thermally activated transport data: **a)** An Arrhenius plot of the conductivity as a function of  $T^{-1}$  for  $V_g = 60.5$  V. The fit is consistent with thermally activated transport. The units of S/1S represent a ‘dimensionless conductance’ for purposes of taking a logarithm. **b)** The extracted activation energy for different gate voltages (each point is an average over an 0.2 V range). . . . . 120
- 6.6 **a)** The  $\sigma(T)$  dependence at  $V_g = 60.5$  V plotted as a function of  $T^{-p}$ , where  $p$  takes the value of 1 for NNH, 1/2 for Efros-Shklovskii VRH, 1/3 for Mott VRH in 2D. The best fit was determined to be  $p = 1/3$ . **b)** The red curve is a plot of  $\sigma(V_g)$  at  $T = 4.2$  K; the overlaid blue data points are extracted values of the hopping parameter  $T_0$ . . . . . 121
- 6.7 **a)** 4-layer WS<sub>2</sub> on h-BN. Top panel: A stability diagram of the differential conductance as a function of source drain voltage and gate voltage at  $T = 4.2$  K. Bottom panel:  $\sigma(V_g)$  at  $T = 4.2$  K. Inset: Conductance traces as a function of source drain voltage, from the regions labeled A (61.5 V) up to B (62 V) on the main panel. **b)** 4-layer WS<sub>2</sub> on SiO<sub>2</sub>, differential conductance as a function of source drain voltage and gate voltage at  $T = 4.2$  K . . . . . 123

- 
- 6.8 Suspended MoS<sub>2</sub>: **a)** A false colour SEM image of a suspended MoS<sub>2</sub> flake: purple is the etched SiO<sub>2</sub>; yellow is the Au contacts; and green is the flake. **b)** An overview of the field effect transfer characteristic for a range of temperatures. The device is biased at  $V_{SD} = 500$  mV. **c)** Mobility values extracted from the  $I(V_g)$  curves at different temperatures. **d)** A closer look at the low temperature  $I(V_g)$  curves. There appears to be repeatable features up to 20 K, two of which are identified by the dashed lines. . . . . 125
- 6.9 Hopping data: **a)** The conductivity data for different gate voltages plotted in terms of thermally activated transport ( $T^{-1}$ ). Dashed lines are a guide for the eyes to see where the data deviates from the fit. **b)** Conductivity data for different gate voltages plotted in terms of Mott VRH ( $T^{-1/3}$ ). . . . . 126

# Contents

<b>1</b>	<b>Introduction</b>	<b>1</b>
1.1	Emergence of 2D single layered materials . . . . .	1
1.2	This thesis . . . . .	4
<b>2</b>	<b>Theoretical concepts</b>	<b>11</b>
2.1	Crystal structure of graphene . . . . .	11
2.1.1	Tight binding model for monolayer graphene . . . . .	13
2.1.2	Massless Dirac fermions . . . . .	19
2.2	Fluorinated graphene . . . . .	20
2.3	Transition metal dichalcogenides . . . . .	21
2.4	Conduction mechanisms in disordered systems . . . . .	24
2.4.1	Temperature dependence of the conductivity in a lightly doped semiconductor . . . . .	24
2.4.2	Mott variable range hopping . . . . .	27
2.5	Raman spectroscopy . . . . .	31
2.5.1	Raman scattering . . . . .	31
2.5.2	Raman spectrum of graphene . . . . .	33
2.6	Superconductivity . . . . .	35
2.6.1	Cooper pairs and the BCS ground state . . . . .	36

---

2.6.2	Andreev reflection . . . . .	40
<b>3</b>	<b>Device fabrication and measurement techniques</b>	<b>51</b>
3.1	Device fabrication procedures . . . . .	51
3.1.1	Mechanical exfoliation and fabricating a simple transistor structure	51
3.1.2	Methods of suspending atomically thin materials . . . . .	54
3.1.3	Improved performance through annealing . . . . .	61
3.2	Synthesis of fluorinated graphene . . . . .	62
3.3	Characterisation of 2D materials . . . . .	64
3.3.1	Optical contrast of graphene . . . . .	64
3.3.2	Determining the number of graphene layers using Raman spectroscopy . . . . .	67
3.4	Electrical characterisation . . . . .	71
3.4.1	Graphene and constant current measurements . . . . .	71
3.4.2	TMDs and constant voltage measurements . . . . .	72
3.5	Summary . . . . .	74
<b>4</b>	<b>Atomically thin and flexible beta radiation detectors based on fluorinated graphene</b>	<b>79</b>
4.1	Introduction . . . . .	79
4.2	Methods . . . . .	80
4.2.1	Fabrication . . . . .	80
4.2.2	Radioactive source calibration . . . . .	82
4.3	Results . . . . .	84
4.4	Discussion and conclusions . . . . .	87
4.4.1	CVD fluorinated graphene device . . . . .	88

---

4.5	Conclusions . . . . .	91
<b>5</b>	<b>Towards suspended MoRe Josephson junctions with a graphene weak link</b>	<b>95</b>
5.1	Introduction . . . . .	96
5.2	Deposition of superconducting metals . . . . .	96
5.3	Characterisation of MoRe . . . . .	98
5.3.1	Thin channels . . . . .	98
5.3.2	Bulk material . . . . .	102
5.4	Resistance to hydrofluoric acid . . . . .	102
5.5	MoRe Josephson junctions with a graphene weak link . . . . .	104
5.6	Conclusions . . . . .	108
<b>6</b>	<b>The nature of electronic transport in WS<sub>2</sub> and MoS<sub>2</sub></b>	<b>113</b>
6.1	Introduction . . . . .	114
6.2	WS <sub>2</sub> . . . . .	114
6.2.1	Methods . . . . .	114
6.2.2	Results . . . . .	118
6.2.3	Discussion . . . . .	119
6.3	MoS <sub>2</sub> . . . . .	124
6.4	Conclusions . . . . .	127
<b>7</b>	<b>Conclusions and proposals for future work</b>	<b>131</b>

